MIT Libraries | DSpace@MIT

MIT Open Access Articles

On the calculation of boundary-layer parameters from discrete data

The MIT Faculty has made this article openly available. ***Please share*** how this access benefits you. Your story matters.

Citation: Titchener, Neil, Simon Colliss, and Holger Babinsky. "On the Calculation of Boundary-Layer Parameters from Discrete Data." Experiments in Fluids 56.8 (2015): n. pag.

As Published: http://dx.doi.org/10.1007/s00348-015-2024-5

Publisher: Springer Berlin Heidelberg

Persistent URL: http://hdl.handle.net/1721.1/107254

Version: Author's final manuscript: final author's manuscript post peer review, without publisher's formatting or copy editing

Terms of Use: Article is made available in accordance with the publisher's policy and may be subject to US copyright law. Please refer to the publisher's site for terms of use.

Massachusetts Institute of Technology

Noname manuscript No.
(will be inserted by the editor)

On the Calculation of Boundary-Layer Parameters from Discrete Data

Neil Titchener · Simon Colliss · Holger Babinsky

Received: 2nd May 2014 / Accepted: 12th August 2014 (subject to revisions)

Abstract An investigation of the errors inherent in the calculation of integral boundary layer parameters from discrete datasets has been carried out. The primary errors examined were those due to discretization of the velocity profile; distance of the first data location from the wall; and uncertainty in the floor location. A range of turbulent velocity profiles with different shape factors from analytical models and published DNS investigations has been examined.

This analysis demonstrates that the spacing of the first measurement point from the floor is by far the most critical error source. Furthermore, the error is shown to be a function of boundary layer shape factor, and therefore a correction factor chart has been derived. Two alternative methods of estimating integral boundary layer parameters have been examined: wall modeling and a gradient-based formulation. These have both been shown to generate smaller errors than the basic integration approach, although both are susceptible to external influences.

N. Titchener

77 Massachusetts Ave., Building 31-261C, 02139

Tel.: +1 (617) 335 0931

E-mail: nat25@mit.edu

Keywords Boundary Layers · Measurement Techniques · Measurement Uncertainties

1 Introduction

The importance of boundary-layer performance on overall fluid dynamical system performance is well known. Examples of areas where the understanding of the boundary-layer characteristics is crucial include wing, aircraft and other vehicle design, flows in ducts and wind tunnels, and atmospheric flows. The boundary layer profile is traditionally characterized by the displacement thickness, δ^*, the momentum thickness, θ, and the shape factor, H. These parameters, in compressible form, are defined in Equations 1 – 3.

$$\delta^* = \int_0^\infty \left(1 - \frac{\rho u}{\rho_\infty u_\infty}\right) \, \mathrm{d}y \,, \tag{1}$$

$$\theta = \int_0^\infty \frac{\rho u}{\rho_\infty u_\infty} \left(1 - \frac{u}{u_\infty}\right) \mathrm{d}y \,, \tag{2}$$

and

$$H = \frac{\delta^*}{\theta} \,. \tag{3}$$

These parameters are valuable because they allow the boundary layer to be characterized quantitatively, and, as a result, they allow informative comparisons to be made between various boundary layers under a range of scenarios. These parameters are therefore widely used throughout the literature. To effectively calculate and/or compare the behaviour of various boundary layers, it is important to minimize errors in the calculation of the boundary-layer integral parameters.

To compute the boundary-layer integral parameters, Equations 1–3, knowledge of both the velocity, u, and density, ρ, variation across the boundary layer is required. Clearly, any uncertainty in $u(y)$ and/or $\rho(y)$ will lead to an error

in the displacement thickness, δ^*, momentum thickness, θ, and shape factor, H. To avoid the complexity of determining both the velocity and density variation across the boundary layer, the boundary-layer integral parameters can be simplified by neglecting the density variation across the boundary layer. With the assumption of constant density across the boundary layer, $\rho(y) = \rho_\infty$, Equations 1 to 2 yield the *incompressible* or *kinematic* boundary-layer integral parameters, Equations 4 to 6.

$$\delta_{\mathrm{i}}^* = \int_0^\infty \left(1 - \frac{u}{u_\infty}\right) \mathrm{d}y \,, \tag{4}$$

$$\theta_{\mathrm{i}} = \int_0^\infty \frac{u}{u_\infty}\left(1 - \frac{u}{u_\infty}\right) \mathrm{d}y \,, \tag{5}$$

and

$$H_{\mathrm{i}} = \frac{\delta_{\mathrm{i}}^*}{\theta_{\mathrm{i}}} \,. \tag{6}$$

While the premise of constant density across the boundary layer may seem like a restrictive assumption, especially in transonic and supersonic applications, density variations in mildly compressible flows, those with $M_\infty < 2$, tend to have little to no impact on the boundary-layer's velocity profile and/or its behaviour; Winter and Gaudet [1970], Morkovin [1962]. As a consequence, authors such as Winter and Gaudet [1970] advocate the use of kinematic boundary-layer integral parameters, because unlike compressible integral parameters, for a given boundary-layer velocity profile, the kinematic parameters are not a strong function of M_∞; Delery [1985]. This benefit, combined with the difficulty in determining the density variation across the boundary layer, means that the kinematic boundary-layer integral parameters are the most valuable parameters in low-speed, transonic and mildly supersonic flows. For this reason, the analysis presented in this article is restricted to the kinematic (incompressible) boundary-layer integral parameters, which from here on will be referred to simply as the boundary-layer integral parameters.

To calculate the true values of the boundary-layer integral parameters for a given boundary layer, the velocity variation must be known as a continuous function through the boundary layer. Yet, real measurements are unavoidably located at discrete locations away from the wall. This results in a discrete dataset such as that presented in Figure 1. The error associated with interpolation is obviously reduced as the number of data points are increased. In particular, more data points are often collected close to the wall, where the highest velocity gradients typically occur. Most often, this is achieved using a logarithmic spacing in the wall-normal direction. See for example De Graaff and Eaton [2000] and Bailey et al. [2013].

There are circumstances, however, where a high level of resolution is not viable, because of practical limitations to the measurement resolution, especially near the wall. This limitation is especially prevalent in laboratory-scale applied aerodynamic research with turbulent boundary layers at high Reynolds numbers. For example, shock wave / boundary layer interaction experiments (Sawyer and Long [1982], Babinsky et al. [2009], and Colliss et al. [2014]), small-scale propulsion system investigations (Wong [1974], Morris et al. [1992], and Wasserbauer et al. [1996]), investigations pertaining to wing aerodynamics (Keener [1986] and Ashill et al. [2005]), and cascade and single-stage turbomachinery studies (Wheeler et al. [2006] and Goodhand and Miller [2010]). In these instances, boundary layers are typically thin, on the order of millimeters. Additionally, the boundary layers in these flows are very often difficult to access even with the most advanced measurement techniques. Consequently, a fine spacing in the boundary layer may not be possible. To illustrate the difficulty of obtaining high quality and high resolution boundary-layer data, an example of a complex compressible flow is presented schematically in Figure 2. In this example, a separated transonic shock-wave / boundary-layer interaction, it is important to obtain measurements across a wide wall-normal range

in both the viscous and inviscid portions of the flow. The typically small characteristic scale, combined with the complexity of the flow, makes all velocity measurements difficult, especially those close to the wall.

In addition to the error incurred due to interpolation between the available data-points, there is also uncertainty in the position of the measurements with respect to the wall, i.e., an error in the wall-normal coordinate, y. Such a bias error in y, Δy_0, is illustrated schematically in Figure 1(b). Due to the need to include the no-slip condition in the calculation of the integral parameters and the high-velocity gradients near the wall, care needs to be taken to precisely determine the location of the wall/surface.

Lastly, there is uncertainty in determining the location of the boundary-layer edge, as shown in Figure 1(c). In practice, although the definition of the displacement thickness, δ_{i}^* and the momentum thickness, θ_{i}, requires integration to infinity, $y \to \infty$, the upper integration limit is set to the boundary layer edge, $y = \delta$, where the boundary-layer thickness is typically defined as the 99% or 99.5% thickness. Hence the contribution of data-points above this location is negligible. Typically, the error introduced by uncertainty in the boundary-layer thickness is at the very least an order of magnitude smaller than the two sources of error discussed above. This third source of error is only briefly discussed, largely for completeness.

In addition to the three sources of error detailed in the paragraphs above, there will, of course, be uncertainty inherent in the measured velocity at each measurement location. This uncertainty will clearly have an impact on the boundary-layer integral parameters. Unfortunately, such errors are a strong function of the experimental setup—both the specifics of the measurement technique and the experimental configuration—and it is therefore difficult to generalize their influence. Fortunately, in the era of prevalent advanced measurement techniques such as Laser Doppler Velocimetry (LDV) this source of

error is not as significant as it once was. For these reasons, this source of error is not included in the following discussion.

An illustrative example of the confusion that can be introduced by errors in the boundary-layer integral parameters is presented in Figure 3. Here, experimentally measured profiles of a boundary layer on either side of a suction slot are shown from Colliss et al. [2014]. In this investigation, a slot was used to remove a portion (approximately 10%) of the boundary layer entering the wind tunnel test section. The measurements of the boundary layer upstream and downstream of the suction slot were achieved using a state-of-the-art LDV system. From these velocity data, the boundary-layer integral parameters were calculated using the standard trapezium based integration method. The resulting quantities are presented in the Table included in Figure 3. Looking at the values of the boundary-layer integral parameters in this Table, it is evident that although the calculated displacement and momentum thicknesses, $\delta^*_{\mathrm{iCALC}}$ and θ_{iCALC}, decrease across the suction slot as expected, the calculated shape factor, Hic, remains largely unchanged. Thus, quantitatively, there appears to be no improvement in boundary-layer health. Yet, this is surprising given the removal of the near-wall, low velocity flow and the marked increase in the 'fullness' of the velocity profile across the slot. See Figure 3. It is suspected that the error incurred in the calculated shape factor, H_{iCALC}, is responsible for the failure of the numerical values to represent the improvement in boundary-layer 'health' and hence resistance to boundary-layer separation.

The difficulty in determining the true boundary-layer integral parameters, and hence true boundary-layer characteristics, makes it difficult to quantify the boundary-layer behaviour in a given flow-field. Furthermore, these difficulties make it hard to compare experiments on nominally similar flow phenomena, especially when the investigations have either been conducted in different facilities or conducted in identical facilities but using different techniques. Compar-

isons with boundary-layer integral parameters calculated from computational fluid dynamics (CFD) can also be troublesome. Consequently, comparisons and conclusions can be misleading if experimental datasets are not corrected for the aforementioned deficiencies.

It is clear that determining the errors due to sampling, wall position, and boundary-layer thickness is important. The aim of this paper is to quantify these errors in the boundary-layer integral parameters calculated from discrete velocity measurements, so that the true boundary-layer integral parameters can be accurately estimated.

In order to rigorously access the impact of measurement resolution on boundary-layer measurements, an analysis is first performed on a theoretical, zero-pressure-gradient, quasi-equilibrium, turbulent boundary layer, which represents an idealized velocity profile, free from random or bias error. The analysis is then generalized to any boundary-layer profile shape with the help of data predominantly from Direct Numerical Simulation (DNS). In the third part of the article, two alternative methods for estimating the boundary-layer integral parameters are discussed.

2 Error analysis on a boundary layer with uniformly spaced velocity measurements

2.1 Zero-pressure-gradient turbulent boundary layer

Before the error in the boundary-layer integral parameters for a particular profile can be quantified, the profile must be known *a priori*. Thus, we begin by deriving an analytical, flat-plate, zero-pressure-gradient, quasi-equilibrium, turbulent boundary layer from experimental measurements of a Mach 1.4 turbulent boundary layer. The experimentally measured boundary layer data and the corresponding analytically derived profile are shown in Figure 4. The boundary-layer measurements in Figure 4 are taken from Titchener [2013]. The continuous velocity profile in Figure 4 was constructed from the experimental data-points using a combination of the Sun and Childs' [1973] model for the log-law and wake regions, and Musker's [1979] model for the sub-layer and buffer region. To account for compressibility a van Driest [1951] transformation has been integrated in both parts of the model. The free parameters of the combined model which define the fit are the skin-friction coefficient, C_{f}, and the boundary-layer thickness, δ. The skin-friction coefficient and boundary-layer thickness are established by first curve-fitting the Sun and Childs' [1973] model to the experimental data. The calculated skin-friction coefficient, C_{f}, is then utilized in the Musker's [1979] formula.

The experimentally measured data-points and corresponding analytically derived profile presented in Figure 4 are shown in both linear and logarithmic coordinates. Examining Figure 4, it can be seen that very good agreement between the experimental data and the model is achieved. It can therefore be concluded that this compound analytical profile is a suitable baseline on which to base the following analyses. At this point, we relinquish the exper-

imental data-points as they are no longer required; all the following analysis will be performed on the analytically derived profile, which will be resampled as if measured experimentally. Initially we will assume for simplicity that our boundary layer of interest is to be uniformly sampled at N equally spaced, wall-normal locations, as if measured discretely by LDV, a hot-wire, or a Pitot-static probe. Such a resampling results in N discrete data-points: Data from $y = \delta/(N-1)$ to δ with a constant spacing of $\Delta y = \delta/(N-1)$ plus the no-slip condition. The sampled data-points, together with $u(0) = 0$, are used to calculate the boundary-layer integral parameters as a function of the number of samples, N, by numerical integration using the trapezium rule. In the remainder of this article, the total number of points within $y \leq \delta$, N, will be referred to as the measurement resolution. The trapezium rule is exclusively employed in this investigation because of its robustness; in particular its use is not constrained to any particular data-point distribution, unlike many one-dimensional integration methods.

The error in the boundary-layer integral parameters obtained by resampling the data at discrete points for various measurement resolutions, N, is presented in Figure 5. In this figure, the error in the displacement thickness, $\Delta_{\delta^*_{\mathrm{i}}}$, momentum thickness, $\Delta_{\theta_{\mathrm{i}}}$ and shape factor, $\Delta_{H_{\mathrm{i}}}$, is shown versus uniform measurement resolution, N. As expected, the error on each parameter decreases with increasing resolution, and each parameter asymptotes to its true value as the measurement resolution, N, tends to infinity. For $N = 150$ there is only a 1% maximum error, whilst for $N = 600$ all parameters are accurate to within 0.001%. Yet, for practical measurement resolutions, $N \leq 50$, it can be seen in Figure 5 that appreciable errors are present in the displacement thickness, momentum thickness and shape factor: A 5% error, which is not an unreasonable level of accuracy, is highlighted in Figure 5 for reference. It can be seen that the number of measurements required to achieve an error level

of less than 5% on all boundary-layer integral parameters, $N_{5\%}$, the boundary layer must be sampled at almost 50 uniformly spaced locations, $N_{5\%} = 50$, with the shape factor being the limiting variable on the sampling requirement.

The reason why the calculated shape factor, H_{iCALC} is the limiting parameter for a given error level (in this example 5%) is apparent from the behaviour of the calculated displacement thickness, $\delta^*_{\mathrm{iCALC}}$, and momentum thickness, θ_{iCALC}, with finite sampling as shown in Figure 5: It can be seen that the displacement thickness, δ^*_{i}, is over-predicted for all measurement resolutions, N; whilst, conversely, the momentum thickness, θ_{i}, is always underestimated. Consequently, the calculated shape factor, H_{iCALC}, will tend to be highly over-predicted, and hence have the largest error of the boundary-layer integral parameters. With a low number of uniformly spaced measurements, $N < 50$, it is easy to see how the state of the boundary layer could be misinterpreted.

2.2 General turbulent boundary layer

The analysis in Section 2.1 is evidence that the error associated with the calculation of boundary-layer integral parameters can be significant. But it should be remembered that the analysis presented thus far is only valid for the zero-pressure-gradient turbulent boundary layer case presented in Figure 4. In practice, the boundary layer of interest will vary widely in character, between applications, primarily due to the action of pressure gradients. To make our analysis analysis more valuable it needs to be extended to a wide range of boundary layer profiles. Due to the inherent error in experimental data, as discussed above, it was decided that the best source of boundary-layer data for a more general analysis is data from Direct Numerical Simulations (DNS). For this reason, a number of datasets from previously published DNS investigations were collated and analyzed by the same method as Section 2.1. A full list of

the data-sets employed for this analysis are shown in Table 1. These DNS solutions provide us with data for a wide range of shape factors, H_{i}, as well as equilibrium and non-equilibrium profiles. To widen the range of shape factors examined further, a number of boundary-layer profiles have been generated for use alongside the DNS in the following analysis. The non-DNS profiles were produced using the analytical compound profile (Sun and Childs [1973] and Musker [1979]), introduced in Section 2.1 and presented in Figure 4, with the skin-friction coefficient, C_{f}, as a free variable.

As in the analysis of Section 2.1, the minimum measurement resolution required to give a 5% error or better on all the parameters, $N_{5\%}$, will be used as our desired error datum. Preliminary analysis of the data demonstrated that the calculated shape factor, H_{iCALC}, carries the largest error of the three integral parameters for all the boundary layers of the data-sets in Table 1. Hence, $N_{5\%}$ represents the minimum sampling requirement for a 5% error in the displacement thickness, δ_{i}^{*}, momentum thickness, θ_{i}, and shape factor, H_{i}. The minimum measurement resolution required to give a 5% error in shape factor, $N_{5\%}$, is plotted against true shape factor, H_{i}, for each of the profiles provided by Table 1 in Figure 6.

A trend is visible in Figure 6: The critical measurement resolution, $N_{5\%}$, exhibits a clear inverse relationship with shape factor, H_{i}, that varies particularly strongly at low shape factors. This inverse relationship is illustrated by the curve-fit that has been included in Figure 6. The unmistakeable trend between $N_{5\%}$ and H_{i} is a highly valuable finding, because it means that the error resulting from discrete data resolution, $\Delta_{H_{\mathrm{i}}}$, can be parameterized by the shape factor, H_{i}. In other words, $\Delta_{H_{\mathrm{i}}} = \mathrm{fn}(H_{\mathrm{i}}, N)$. Using this methodology, the true shape factor, H_{i}, can be obtained from the sample velocity data. The inverse relationship exhibited in Figure 6, which only shows the required sampling for a 5% error, is also observed when the analysis is repeated at other

error levels. Curves for a variety of uncertainty limits, from 0.5% to 20%, are presented in Figure 7. In Figure 7, It can be seen that the inverse relationship between the critical measurement resolution and shape factor exists for any given error level: The critical sampling density, $N_{5\%}$, decreases with increasing shape factor, H_{i}. As a result of Figures 6 and 7, it can be concluded that the error will be reduced with either higher shape factor (H_{i} or H_{iCALC}) and/or when the overall uniform measurement resolution, N, is increased.

On the basis of the trends produced in Figures 6 and 7, it is possible to determine the error due to uniform sampling resolution as a function of the calculated shape factor, H_{iCALC}. Consequently, from knowledge of the measurement resolution, N, and the estimate of shape factor from the discrete data, H_{iCALC}, a correction factor may be obtained*. The resulting correction factor is presented graphically by a family of curves in Figure 8.

In Figure 8, each curve represents a different measurement resolution (uniformly spaced), which is a known characteristic of the dataset. To obtain the appropriate correction factor, the measured profile is integrated numerically to give a first estimate of the shape factor H_{iCALC}. For a given H_{iCALC} each curve has two corresponding values of the calculation error due to the shape of the error curves—most noticeable in Figure 8(a). The appropriate part of the curve, the lower section, must be selected to establish the error on the boundary-layer shape factor. For example, if $H_{\mathrm{iCALC}} = 1.80$ and $N = 12$, the error is either 10% (corresponding to $H_{\mathrm{i}} = 1.60$) or 40% (corresponding to $H_{\mathrm{i}} = 1.25$). The correct level of error is 10% giving the true value of the boundary-layer shape factor as $H_{\mathrm{i}} = 1.60$.

When applying the correction factor method, it is estimated that the error due to limited measurement resolution can be reduced to within 1% for most

*it was found that plotting H_{iCALC} against H_{i} produced curves which were too closely-spaced to be of practical use

boundary-layer profiles based on a regression fit analysis of the data in Figure 6 (excluding other sources of error).

It is important to remember that the analyses presented in this section assume uniformly spaced data points. To maintain a uniform distribution of data points, the spacing between points is decreased as the number of samples, N, is increased. Yet, a uniform distribution of points is not necessarily realizable, or desirable, under many experimental conditions. Consequently, the levels of errors presented above are unlikely to be valid for the majority of experimental investigations. For this reason, the analyses are expanded to more realistic data-point distributions in the next section, Section 3.

3 The importance of wall offset, near-wall data-points and more realistic data-point distributions

Looking back at Figure 1, it is evident that it is not only the discretization of the boundary layer that introduces errors on the integral parameters. A second source of error is introduced by uncertainty in the position of the measurement location relative to the wall, y. This distance, y, may be uncertain due to mechanical inaccuracies in the traverse gear or alignment procedure; non-uniform surfaces; or flexure of the surface in question. To examine the significance of a potential wall misalignment, a wall offset, $\Delta y_0/\delta$, has been added to the analytical zero-pressure-gradient boundary layer profile shown in Figure 4 to simulate a misalignment of the experimental apparatus. Such a theoretical misalignment represents a case where the spacing between points within the traverse is known, but their distance relative to the wall has an associated bias error. In other words, the wall-normal displacement of each velocity measurement is shifted by an amount $\Delta y_0/\delta$. For comparative purposes, the discretization remains unchanged. Furthermore, the error level associated with the discretization—as calculated by the analysis presented in Section 2—has been subtracted to isolate the floor misalignment error. The results of this analysis are presented in Figure 9.

Examining Figure 9 it is visible that even small misalignments in the floor location have a significant impact on the error in the boundary-layer integral parameters. For example, if all the points in the boundary layer are shifted by $\Delta y_0/\delta$ = +0.01, in other words, the wall location is 0.01δ lower than the experimentalist believes it is, there is an error in the calculated value of the kinematic displacement thickness of 6% ($\Delta_{\delta_{\mathrm{i}}^*}$ = 5.9%), an error in the kinematic momentum thickness of 1.5% ($\Delta_{\theta_{\mathrm{i}}}$ = 1.3%) and an error in the kinematic shape factor of 4.5% ($\Delta_{H_{\mathrm{i}}}$ = 4.5%). It is worth noting that the displacement

thickness, δ_{i}^{*}, is most susceptible to wall misalignment errors, since its integrand $f_{\delta_{\mathrm{i}}^{*}} = 1-(u/u_{\infty})$, has its maximum value at the wall, $y/\delta = 0$. In contrast, the momentum thickness integrand, $f_{\theta_{\mathrm{i}}} = (u/u_{\infty})(1-u/u_{\infty})$, has its maximum at $u(y) = u_{\infty}/2$. For this reason, the displacement thickness is most sensitive to wall misalignment. In Figure 9, the linearity of the wall misalignment errors is also visible. Such behaviour is to be expected when utilizing a linear interpolation scheme, such as the trapezium integration method.

The preceding discussion highlights the relative importance of the near-wall region in the determination of the boundary-layer integral parameters. As a consequence, it is appropriate to turn our attention to the relative significance of sampling errors close to the wall. To illustrate the importance of the data in the near-wall region, we will specifically focus on the first data-point from the wall, more specifically its distance from the wall, y_1. The contribution of the position of the first data-point, y_1, to the total error in boundary-layer shape factor, $\Delta_{H_{\mathrm{i}}}$, has been evaluated for all the profiles in Table 1 by performing two error calculations: The first with the data sampled by $N = 50$ uniformly spaced points and second with a linear interpolation between $y = 0$ and $y = y_1 = \delta/(N-1)$ and the exact profile for $y > y_1$. The difference between the two resulting values of the shape factor gives us an estimate of the contribution of the position of the first data-point to the overall discretization error. The results of this analysis are plotted against the shape factor in Figure 10, where the contribution to the total error of the first data-point, $\Delta_{H_{\mathrm{i}}y_1}/\Delta_{H_{\mathrm{i}}}$, is plotted against the true shape factor, H_{i}. From Figure 10, it can be seen that interpolation to the first data-point contributes the majority of the total error—more than 70%—for all shape factors. What is more, the contribution tends to increase for the smaller shape factors (which also have the largest errors), reaching more than 90% of the total error for velocity profiles with the lowest shape factors.

The significance of the position of the first velocity measurement from the wall, y_1, can be highlighted further by plotting the wall-normal variation of the numerical integration error, i.e., the error introduced by interpolating the integrand of the parameter in question ($f_{\delta_i^*} = 1 - u/u_\infty$ and $f_{\theta_i} = (u/u_\infty)(1 - u/u_\infty)$) with straight lines. In the case of uniform spacing, with the distance between adjacent points given by Δy, it can be shown via some mathematical manipulation (see Appendix A for full details) that the numerical error in the displacement and momentum thickness is given by Equations 7 and 8 respectively:

$$\varepsilon_{\delta_i^*}(y) = -\frac{\Delta y^3}{12u_\infty}\frac{\partial^2 u}{\partial y^2}\,, \tag{7}$$

and

$$\varepsilon_{\theta_i}(y) = \frac{\Delta y^3}{12u_\infty^2}\left(\frac{\partial^2 u}{\partial y^2}(u_\infty - 2u) - 2\left(\frac{\partial u}{\partial y}\right)^2\right). \tag{8}$$

In Figure 11 the contribution to the total error as a function of wall-normal distance, y, as calculated using Equations 7 and 8 is presented for three boundary-layer profiles with different kinematic shape factors. Noting the logarithmic scale on the ordinate, it is clear that the greatest contribution to the total error occurs close to the wall in all cases. In addition, it is apparent that this phenomenon is exacerbated as the shape factor decreases. Furthermore, Figure 11 demonstrates that as the shape factor is decreased, the region of primary error moves closer to the wall. Figure 11 illustrates that it is not the sampling rate which is of primary importance, but rather the position of the first point away from the wall, where in this analysis $y_1 = \delta/(N-1)$. Indeed, any data gathered above $y/\delta \gtrsim 0.05$ is insensitive to the discretisation. See Figure 11. The measurements towards the boundary-layer edge are not

very influential. This signifies that determining the boundary layer thickness accurately is not necessary †.

Figures 9, 10, and 11 demonstrate that the wall-proximity of the first data point is the most important aspect in determining the error in the boundary-layer integral parameters. This fact has a number of consequences for our analysis. Up until now, by considering only uniform sampling, we have been indirectly setting the location of the first data-point from the wall at $y_1 \equiv \delta/(N-1)$. However, the position of the first data-point is not typically determined by the overall sampling rate, but, in fact, by experimental limitations such as the presence of reflections (in the case of optical boundary-layer measurement techniques) and/or geometric restrictions (in the case of Pitot probes or hot-wires). Consequently, it necessary to reformulate the correction technique presented in Figure 8 to be more relevant to experimental data-sets.

To maximize the relevance of this article's analysis, the correction technique introduced in Section 2 needs to be reformulated so that the error correction can be based on the non-dimensional position of the first data-point from the wall, y_1/δ, instead of the number of samples, N. To keep the analysis simple enough to retain a graphical look-up chart, much like Figure 8, we retain a two degree-of-freedom problem based on shape factor, H_{i}, and the position of the first data-point, y_1/δ. As a result, we restrict the analysis to only consider the integration error between the wall and the first data-point‡. Nonetheless, the insensitivity of the error due to sampling in the outer portion of the boundary layer, as presented in Figure 11, demonstrates that such a simplification is valid for all but the lowest measurement resolutions above the position of the first velocity measurement $u(y_1)$.

†While the determination of the boundary-layer thickness is not crucial for the integral parameters its accurate determination is certainly useful for other comparative purposes

‡In the analysis, the number of samples above y_1 was set to 600 which approximates a continuous profile

Implementation of an analysis based on the first data-point, y_1, instead of the overall measurement resolution, N, leads to the data that is presented in Figure 12. In this figure, the error in the true shape factor, Δ_{H_i}, as a function of the calculated shape factor, H_iCALC, for various wall-normal proximity of the first measured data-point, y_1/δ, is shown graphically.

Figure 12, much like Figure 8, can be used to estimate the true shape factor, H_i from the calculated shape factor, H_iCALC and the location of the first measurement from the wall, y_1/δ. Similarly to the original look-up chart presented in Figure 8, using the look-up chart of Figure 12, the true boundary-layer shape factor, H_i can be estimated to within 1% without the requirement to collect data in close proximity to the wall. Figure 12 allows the error incurred as a result of experimental limitations to be estimated and largely negated in cases where y_1/δ 'is limited'.

Unlike Figure 8, Figure 12, shows that a high sampling rate (especially at low shape factors) is no longer a requirement to achieve a small error, or equivalently a large correction factor. This is advantageous because, as previously discussed, the measurement resolution, N, required to give acceptable error levels (5% or better) without introducing a correction is approximately fifty data-points, $N_{5\%} = 50$, which is unviable in many applications.

Up until this point, our discussion has been largely limited to instances with uniformly spaced data-points. However, it is not uncommon for experimental investigations to use logarithmically spaced points to account for the higher velocity gradients in the near-wall region—see, for example, De Graaff and Eaton [2000]. To examine the benefit of adopting such a non-uniform spacing, the analytical profile developed in Figure 4 was sampled with fifty data-points, $N = 50$, with the position of the first data-point, y_1/δ, a free variable such that $y_0 = 0$, y_1 is variable, and the remaining data-points, y_2–y_N, were spread both uniformly and logarithmically up to the boundary-layer edge, $y = \delta$. A

comparison of the errors on the boundary-layer integral parameters as a result of uniform and logarithmic spacing is shown in Figure 13(a).

Across the range of y_1/δ shown in Figure 13(a), there is little discernible difference between the cases employing linear and logarithmic spacing. Only when the first data-point, y_1, falls below 1% of the boundary-layer thickness, $y/\delta < 0.01$, is there a clear benefit to the logarithmic spacing—including a physical trend towards zero error as y_1 tends to 0. It is clear from Figure 13(a), however, that the advantage is only noteworthy at very small y_1, and, unfortunately, such distances are much closer to the wall than is realisable in many applied aerodynamic investigations.

The potential benefit of employing logarithmic spacing is demonstrated in more general form in Figure 13(b). In Figure 13(b), the critical position of the first data-point required to give a 5% error in all boundary-layer integral parameters, $y_{1(5\%)}/\delta$, as a function of the measurement resolution, N, is shown. For example, for a measurement resolution of fifty, $N = 50$, Figure 13(a) shows that the largest error in boundary-layer integral parameters passes 5% when $y_1/\delta = 0.021$, which yields the corresponding point in Figure 13(b), $y_{1(5\%)}/\delta = 0.021$. Performing a similar analysis at various measurement resolutions, N, for both uniform and logarithmic spacing, leads to the curves in Figure 13(b).

It is apparent from Figure 13(b) that above a certain number of data points, the critical position of the first velocity measurement required to give a maximum error of 5%, $y_{1(5\%)}/\delta$ is independent of the measurement resolution, N. This occurs at approximately 40 data-points in the case of linear spacing and at approximately 20 in the case of logarithmic spacing. Below a measurement resolution of forty, $N < 40$, there is an advantage to employing logarithmically spaced data-points. At low measurement resolutions the interpolation between data-points, and not just the interpolation between the first data-point, y_1, and the wall, is significant. The advantage of logarithmic

spacing can also be achieved by clustering a handful of data-points near to the wall, based on the resolution of your measurement technology. If it is possible to achieve 30–40+ data-points there is no advantage to employing logarithmic spacing: Whether uniform or logarithmic spacing is utilized, the position of the first data-point, y_1, dominates the error in the boundary-layer integral parameters. The error correction chart presented in Figure 12 is useful whether uniform or logarithmic spacing is utilized.

In summary, the first point from the wall, y_1/δ, is the key parameter in determining the error in the kinematic boundary-layer shape parameter due to the unavoidable discrete nature of experimental data-sets. We should always strive to improve the near-wall resolution of our measurement technologies, but in instances where even the best measurements lie more than 0.01δ above the wall, the correction methodology presented in Figure 12 can be used to gain a better estimate of the true boundary-layer integral parameters.

4 Alternative calculation methods

4.1 Wall modeling

The analysis in Section 3 demonstrates that the most significant contributor to the error inherent in the numerical integration is data (or more precisely a lack of data) in the near-wall region. One method to overcome this deficiency is to add data-points near the wall using a wall model. There is general agreement that very close to the wall, where turbulence is damped out, the velocity profile is linear. See Lindgren [1965] and White [2006]. In other words:

$$\tau_{\mathrm{w}} = \mu_{\mathrm{w}} \frac{u}{y} \,, \tag{9}$$

which, with the introduction of the wall-shear stress and some rearrangement, leads to

$$\frac{u}{u_\tau} = \frac{\rho_\mathrm{w} y}{\mu_\mathrm{w}}, \tag{10}$$

or, simply,

$$u^+ = y^+ \ . \tag{11}$$

The region in which Equation 11 is valid is generally accepted to be up to a non-dimensional wall-distance based on inner-variables of 5, $y^+ = 5$. This region, $y^+ \leq 5$, is referred to as the sub-layer.

To implement this wall model, however, the skin-friction velocity, u_τ, must be estimated. To do this, the experimental data can be fitted to the log-law region,

$$u^+ = (1/\kappa)\log(y^+) + B \ , \tag{12}$$

using a least squares method to determine the wall-friction velocity, u_τ—much like a Clauser plot. For compressible flows, a modified form of the log-law is appropriate, often referred to as a van Driest [1951] transformation. Once the skin-friction velocity, u_τ, has been estimated velocity data from the wall model can be added in the sub-layer to complement the experimental data. Since the sub-layer velocity profile model is linear and in this instance the trapezium rule method of integration is being used, the only data-point that needs to be added to the experimental data is the velocity at the edge of the sub-layer, which we will include at $y^+ = 5$. This leads to the data-point

$$(y, u) = (5\nu_w/u_\tau, 5u_\tau) \ , \tag{13}$$

which is then added to the experimental data. The calculation of the integral boundary layer parameters then proceeds as before.

To illustrate how the introduction of this wall model can help to reduce errors in the calculation of the boundary-layer integral parameters, the error in the boundary layer integral parameters for the zero-pressure-gradient analytical boundary-layer of Section 2.1 and Figure 4 is once again calculated, but this time with the inclusion of the wall model.

The variation of the error incurred in the calculated displacement thickness, $\Delta_{\delta_{\mathrm{i}}^*}$, momentum thickness, $\Delta_{\theta_{\mathrm{i}}}$, and shape factor, $\Delta_{H_{\mathrm{i}}}$, as a function of the measurement resolution, N, are shown in Figure 14 [§]. For comparative purposes, the corresponding curves in the absence of any modeled data, from Figure 5, are included in Figure 14 as dashed lines.

Comparing the errors in the boundary-layer integral parameters with and without the wall model in Figure 14, it is visible that the inclusion of the wall model has led to a substantial reduction in the errors in all boundary-layer integral parameters relative to the standard method of calculating the boundary-layer integral parameters (Section 2). Much like before the shape factor H_{i} remains the variable with the greatest overall error (an over-prediction). Once again, an error of 5% is chosen as our desired error level. Whilst, for the unmodified profile, the minimum measurement resolution to achieve the 5% error is fifty, $N_{5\%} = 50$, for the wall modeling method, this is reduced to thirty data-points, $N_{5\%} = 30$. Thus for a typical experimental dataset such as that of Titchener [2013], in which the measurement resolution of the boundary-layer measurements was typically thirty, $N \approx 30$, the error in the boundary-layer integral parameters would be within 5% of their true value if a wall model had been included.

[§]Note that the additional wall modelled point is not included in the definition of the measurement resolution, N.

Extending the analysis to boundary layers with various velocity distributions, the DNS data has once again been sampled but this time simultaneously combined with the wall model. Once more, the measurement resolution required to achieve 5% error or less in all the boundary-layer integral parameters, $N_{5\%}$, has been calculated for each of the profiles provided by the data-sets of Table 1. The result of such an analysis is presented in a similar fashion to Figure 6 in Figure 15, where the critical measurement resolution for a 5% error, $N_{5\%}$, is plotted versus true shape factor, H_{i}. In Figure 15 the curve-fit to the data from the standard method of Figure 6 is reproduced for comparative purposes. What is apparent from Figure 15 is that the reduction in the measurement resolution requirement for a 5% error level, $N_{5\%}$, is realized at any shape factor, H_{i}. This is a useful result as it means that no restriction is required as to when the simple wall modeling method can be applied. Comparing the curve-fits for the boundary-layer data with and without the wall model in Figure 15, it can be seen that the trend with shape factor, H_{i}, is very similar with or without modeling, i.e., the error is much more sensitive to measurement resolution for the lower shape factors. This is not an unexpected result given that the fundamental characteristics of the evaluation method are unchanged by wall modeling.

It should be remembered that to implement the wall-model method, the skin-friction velocity, u_τ, must be estimated. Hence, any error in this estimation should not be neglected, as an error in the skin-friction velocity, Δ_{u_τ}, will propagate as an additional error source to the boundary-layer integral parameters. It is not within the scope of this article to examine the factors that influence the wall-friction velocity, u_τ, or quantify their magnitude. For a detailed account on estimating the wall-friction velocity and any associated uncertainty, the reader should refer to Kendall and Koochesfahani [2008], Örlü et al. [2010], and Rodriguez-López et al. [2015].

The magnitude of the error in the skin-friction velocity, Δ_{u_τ}, in high Reynolds number laboratory-scale wind tunnel investigations cannot be generalized as its magnitude will depend strongly on the specifics of the experimental setup in question. However, it is possible to obtain a first approximation for the influence of an error in the wall-friction velocity, Δ_{u_τ}, by examining the sensitivity of the boundary-layer integral parameters to the wall-friction velocity by imposing an artificial error in the skin-friction velocity, Δ_{u_τ} and then evaluating the resulting change in shape factor, H_{i}. To this end, curves of the error incurred in the shape factor, $\Delta_{H_{\mathrm{i}}}$, versus measurement resolution, N, for two profiles with different shape factors, H_{i} = 1.30 and H_{i} = 2.52, are shown in Figure 16(a) and (b), respectively. The various curves in each figure represent different error levels in the skin-friction velocity Δ_{u_τ}, used to implement the wall modeling method. By comparing the differences in the various curves in Figure 16 to the overall error in calculated shape factor, H_{iCALC}, at a given measurement resolution, N, it is visible that the contribution to the total error due to the uncertainty in the skin-friction velocity, u_τ is small. For example, when calculating the integral parameters of a H_{i} = 1.30 profile using a dataset sampled by fifteen data-points, N = 15, an error of 10% in the skin-friction velocity, Δ_{u_τ} = 10%, contributes 1.25% to the overall error of 14%, $\Delta_{H_{\mathrm{i}}}$ = 14%. For a H_{i} = 2.52 profile sampled with the same measurement resolution, N = 15, an error of 10% in the skin-friction velocity,Δ_{u_τ} = 10%, contributes 0.7% to the overall error of 2%, $\Delta_{H_{\mathrm{i}}}$ = 2%. Thus, even with an uncertainty of 10% in the value of skin-friction velocity, u_τ, the wall modeling method represents a vast improvement over the standard method presented in Section 2.

In principle a look-up correction chart of correction factors much like Figure 12 can also be generated for the approach including the wall model. However, the error incurred in the boundary-layer integral parameters across a wide

range of shape factors, H_{i}, and measurement resolutions, N, is potentially low enough—the error is less than 10% for all but the lowest shape factors above a measurement resolution of twenty, $N > 20$—to not warrant using a look-up chart. Solely employing the wall model is also attractive because it is based on physical observations and scaling arguments as opposed to the standard correction method in Section 2 which employs a semi-empirical correction factor. As a result, it is suggested that in cases where a good approximation of the skin-friction velocity can be made, it is beneficial to include the wall model in the calculation of the boundary-layer integral parameters.

Whether or not the wall-model is employed in the calculation of the boundary-layer integral parameters, the introduction of near-wall data-points, once again, highlights the importance of velocity data close to the wall.

4.2 Gradient based parameters

Instead of adding data-points near the wall, an alternative method of improving the calculation of the boundary-layer integral parameters is via a gradient-based formulation. If we integrate by parts and employ the boundary conditions $u(y > \delta) = u_\infty$ and $u(y = 0) = 0$, the standard definitions of displacement thickness, δ_{i}^* and momentum thickness, θ_{i}, Equations 4 and 5, may be rewritten leading to:

$$\delta_{\mathrm{i}}^* = \frac{1}{u_\infty} \int_0^\infty y \frac{\partial u}{\partial y} \mathrm{d}y \tag{14}$$

and

$$\theta_{\mathrm{i}} = \frac{2}{u_\infty^2} \int_0^\infty y u \frac{\partial u}{\partial y} \mathrm{d}y - \frac{1}{u_\infty} \int_0^\infty y \frac{\partial u}{\partial y} \mathrm{d}y \,. \tag{15}$$

This alternative form of the boundary-layer integral parameters is primarily used to avoid ambiguity in defining the boundary-layer edge in cases where

there are strong wall-normal pressure gradients. For example, on the curved surface of an airfoil; Spalart and Watmuff [1993], Colliss et al. [2014]. It might be expected that these alternative formulae will also reduce the calculation errors, since the introduction of the wall normal distance, y, in the integrands of both parameters will reduce the contribution of the near-wall region to the total integral value. Based on this possible benefit, the gradient method was implemented in this study by computing the gradients using centred finite difference approximations, before integrating using the trapezium rule. The results of this analysis for three different boundary layer profiles from the DNS data listed in Table 1 are shown in Figure 17. For the lower shape factors shown in Figure 17(a) and (b), the curves of calculated displacement thickness $\delta^*_{\mathrm{iCALC}}$ exhibit a similar trend to Section 2.1, with the error in the calculated displacement thickness, $\delta^*_{\mathrm{iCALC}}$, inversely proportional to the measurement resolution, N. However, unlike Section 2, the true momentum thickness, θ_{i}, is no longer underestimated, but overestimated. This is a noteworthy and desirable characteristic, because, as a direct consequence, the error in the shape factor, $\Delta_{H_{\mathrm{i}}}$, is significantly reduced relative to the standard integration approach (Section 2) due to a partial cancellation of errors. See Figure 17(a) and (b).

Yet, unlike all prior analysis in this article, the trend observed using the gradient-based approach at low shape factors (H_{i} = 1.30 and 1.62) is not consistent with that at the highest shape factor analyzed, H_{i} = 2.52. In the case of the higher shape factor profile, H_{i} = 2.52, presented in Figure 17(c), both the calculated displacement thickness and momentum thickness, $\delta^*_{\mathrm{iCALC}}$ and θ_{iCALC}, underestimate the true parameters. On the other hand, the observed overestimate in true shape factor, H_{i}, is similar to that produced by the gradient-based approach at low shape factors. Contrary to the standard and wall-model methods, the limiting factor to retain all parameters within a

certain error tolerance is the displacement thickness, δ_{i}^{*}, for low shape factors, $H_{\mathrm{i}} \leq 1.4$, and the momentum thickness, θ_{i}, for higher shape factors, $H_{\mathrm{i}} > 1.4$. Thus, the critical measurement resolution in this case, $N_{5\%}$, is defined as that for which the maximum error in all three parameters is 5% or lower (previously only the error in shape factor, $\Delta_{H_{\mathrm{i}}}$, was considered since this was always the largest). Using this definition, it is once again possible to plot and then curve-fit critical measurement resolution, $N_{5\%}$, against true shape factor, H_{i}. These data are presented in Figure 18. The curve-fit for the standard method of Section 2, which utilizes no modeling or gradient methodology is, once again, included as a dashed line.

Comparing the curve-fits of the error in the calculation of the boundary-layer integral parameters from the standard and gradient based methods in Figure 18, it is apparent that the gradient-based formulation reduces the error in the boundary-layer integral parameters for a given measurement resolution, N. However, there is more scatter in the data of the gradient based approach, compared with the other methodologies—compare Figures 6, 15, and 18. In particular, a small group of points in the range $1.3 < H_{\mathrm{i}} < 1.6$ is seen to lie some distance away from the remainder of the data. These points correspond to favourable pressure gradient (non-equilibrium) boundary layers. The reason that these should depart from the curve requires further investigation; but it is suspected to be linked to increased velocity gradients in the near-wall region.

An advantage of the gradient-based formulation over the wall modeling method is that it does not rely on an estimate of the skin-friction velocity. Yet, the necessity to compute the gradient of measured velocity profiles does make this method susceptible to errors in the original boundary-layer velocity measurements—which are unavoidable. Again, while it is beyond the scope of this paper to generalize the sources and magnitudes of noise introduced by the various techniques for measuring velocity, it is possible to assess the

sensitivity of the gradient-based approach to random Gaussian noise relative to the standard method.

To examine the influence of a velocity profile that includes noise in the initial velocity measurements, a random Gaussian noise signal was generated and added to the sampled boundary layer profiles before the integral boundary-layer parameters were calculated. An example of a noisy boundary-layer profile produced by this method is shown in Figure 19(a). In this example, the magnitude of the noise was set to be 1% of the local velocity, $u(y)$, and this was imposed at every measurement location in the profile except $y = 0$. (Whether this 1% noise level is representative of a typical magnitude and distribution of noise is difficult to verify, but if anything this level of error is thought to underestimate typical velocity measurement errors). The integral parameters of this noisy boundary-layer profile were then calculated using the gradient-based method, Equations 14 and 15, as well as by the unmodified standard integration method, Equations 4 and 5. The random nature of the noise introduced in this analysis causes the resulting error curves to also exhibit random fluctuations. Thus to obtain an average quantification of the effect of noise for each measurement resolution the process of adding a random Gaussian signal and then calculating the boundary-layer integral parameters was repeated 1000 times. The standard deviation of the error in the boundary-layer integral parameters was then calculated based on the 1000 sample profiles. The result of introducing noise before calculating the boundary-layer integral parameters is presented in Figure 19. This figure presented data for a low shape factor, $H_{\mathrm{i}} = 1.30$, boundary-layer.

Examining Figure 19, it is seen that, although the noise level is small, the gradient method incurs a notably large error—particularly in the calculated displacement thickness, $\delta^*_{\mathrm{iCALC}}$ and calculated momentum thickness, θ_{iCALC}: For the noise level introduced here of 1%, it is seen that the integral param-

eters are only reliably accurate to within 10%, even for large measurement resolutions, $N > 50$. In this particular instance, the calculated momentum thickness, θ_{iCALC}, is the limiting factor. By contrast, integration using the standard parameter definitions, Equations 4 and 5, also shown in Figure 19, is much more robust, with little ($\leq 1\%$) excess error introduced by the random noise. It is worth noting that the robustness of the standard approach to noise demonstrated here in Figure 19 verifies our earlier assertion that errors in the velocity measurements are only a small overall contributor to the total error in the boundary-layer integral parameters (as long as the gradient-based approach is avoided).

A successful implementation of the gradient-based approach thus requires the noise inherent in the velocity data to be smoothed out before integration is performed. Once this is done, the computed integral parameters can have an improved error relative to the standard method of Section 2. However, the gradient-based approach cannot be generally recommended due to its susceptibility to noise in the initial boundary-layer velocity measurements (though in certain situations it may be beneficial for alternate reasons).

5 General Recommendations

The above analysis has examined various errors associated with the calculation of kinematic integral boundary layer parameters from discrete data sets. Based on the findings of Sections 2–4, the following method is recommended for minimizing the error in the boundary-layer integral parameters due to the discrete nature of experimental data-sets:

First and foremost, the experiment should be designed such that the position of the first velocity measurement, y_1, is as close to the floor/wall as possible. The number of points between the position of the first measurement,

y_1, and the edge of the boundary layer, δ, is less critical, but somewhere in the range 20–40 is preferable. At the lower end of this range, it is worth employing logarithmic spacing.

Once the boundary-layer profile has been measured, an estimate of the boundary-layer integral parameters should be made using trapezoidal numerical integration (remembering to add the no-slip condition, $u = 0$ at $y = 0$) to estimate the boundary-layer integral parameters, $\delta^*_{\mathrm{i,CALC}}$, $\theta_{\mathrm{i,CALC}}$ and $H_{\mathrm{i,CALC}}$. The best estimate of the true values of the boundary-layer integral parameters, δ^*_{i}, θ_{i} and H_{i}, can then be obtained using the correction factor methodologies presented in this paper.

Of the three possible methodologies for correcting the boundary-layer integral parameters introduced in this article, the basic correction approach introduced in Section 2 and presented graphically in look-up table form in Figure 12 is advocated for widespread use. It is the simplest and the most robust method, as it invokes no additional assumptions and is least susceptible to external errors. Consequently, the authors recommend that this methodology be utilized in the vast majority of instances.

If implemented appropriately, the wall-modeling and gradient based approaches offer the advantage of a much reduced correction factor. In instances where accurate velocity measurements are obtainable in the log-law region, the wall-model method has the potential to be the most preferable option. At the very least, it should be compared to the basic approach. In instances with high wall-normal pressure gradients it is likely to be beneficial to employ the gradient-based approach. When employing either the wall-model or the gradient-based approach a correction chart similar to Figure 12 can be used. Obviously, the most appropriate methodology will vary between applications and the experimental investigator will need to use their own judgement where

calculating the integral parameters. The suggestions made here should only be used as a guideline for experimentalist best practice.

6 Conclusions

An investigation of the error sources inherent in the calculation of boundary-layer integral parameters has been undertaken. The effect of the overall sampling resolution, distance of the first point from the wall, and wall/floor misalignment have been considered. The analysis was performed on boundary-layer profiles obtained from analytical models and DNS investigations.

It has been demonstrated that the error in the boundary-layer integral parameters is significant ($\leq 5\%$) for most data-sets under experimental conditions typically achievable for applied aerodynamic research. Furthermore, it has been shown that the magnitude of the error in the boundary-layer integral parameters is an inverse function of the kinematic shape factor of the velocity profile. In other words, boundary-layer profiles with a low kinematic shape factor require significantly more data-points to achieve a given error level compared to a boundary layer with a high kinematic shape factor. Crucially, the observation that it is possible to parameterize the error in the boundary-layer integral parameters on the true kinematic shape factor has led to to a new error correction methodology using a simple look-up chart/table.

The greatest contribution to the error in the boundary-layer integral parameters is introduced in the region between the wall and the first data-point; errors introduced from data above the position of the first velocity measurement typically account for 10–20% of the overall error. For this reason, a correction factor look-up table based on the position of the first data-point, y_1, was generated. Such a parameterization is thought to be very valuable

because the position of the first data-point, y_1, is typically limited by experimental constraints.

The effect of uncertainty in the wall distance has also been examined. It has been demonstrated that such a misalignment can introduce appreciable errors even for relatively small uncertainties in the wall distance. The magnitude of this error depends strongly on both the shape factor and skin friction coefficient of the boundary layer profile.

Two alternative methods of calculation of the integral parameters have also been investigated: wall modeling and a gradient-based formulation. Both methods can reduce the error in the initial calculation of the boundary-layer integral parameters. However, both are susceptible and therefore sensitive to external influences. Although this sensitivity could not be generalized by the present paper, the effects of both have been demonstrated. Both methods showed promise relative to integration on the original data sets using the standard parameter definitions. Nevertheless both methods would still benefit from a look-up table correction factor, largely mitigating the benefit of adopting either method for the purpose of reducing the calculation errors. Consequently, the authors recommend the use of the look-up chart in Figure 12 as the best method for mitigating the error incurred in the boundary-layer integral parameters caused by discrete boundary-layer data.

Acknowledgments

The authors would like to acknowledge the financial support provided by the Engineering and Physical Sciences Research Council (EPSRC) of the United Kingdom (UK). The authors would also like to thank Todd Davidson and Nina Siu for thoroughly proofreading this article prior to publication.

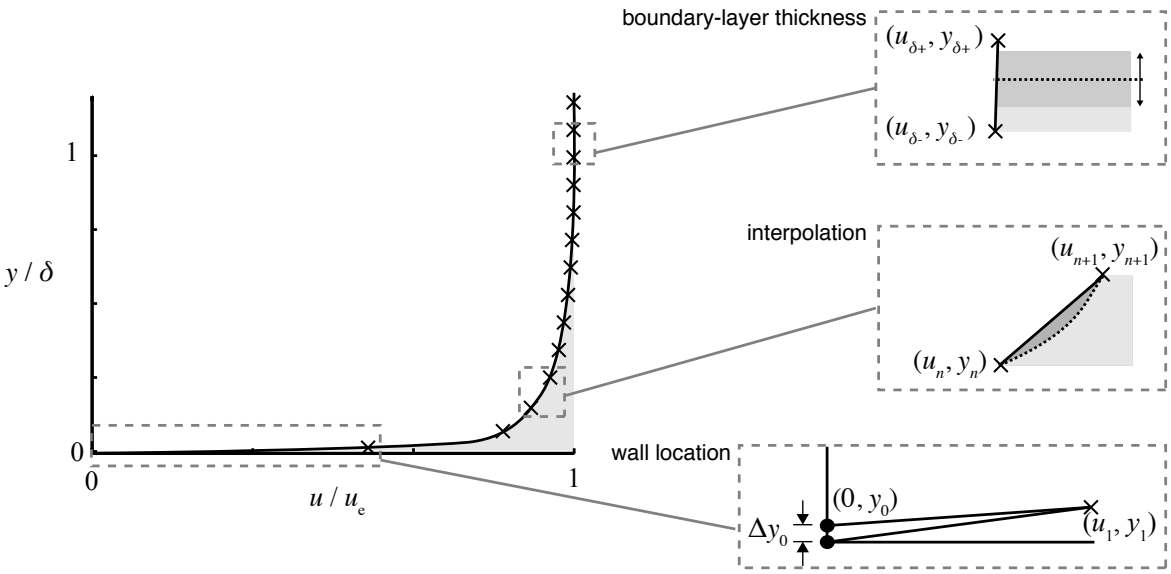

Fig. 1 Potential error sources in boundary -ayer velocity data that leads to errors in the calculation of boundary-layer integral parameters

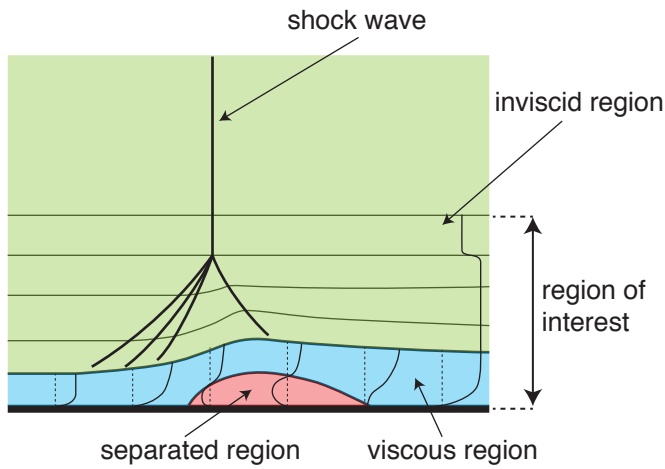

Fig. 2 Schematic illustration of boundary-layer measurements across a terminal shock-wave / boundary-layer interaction

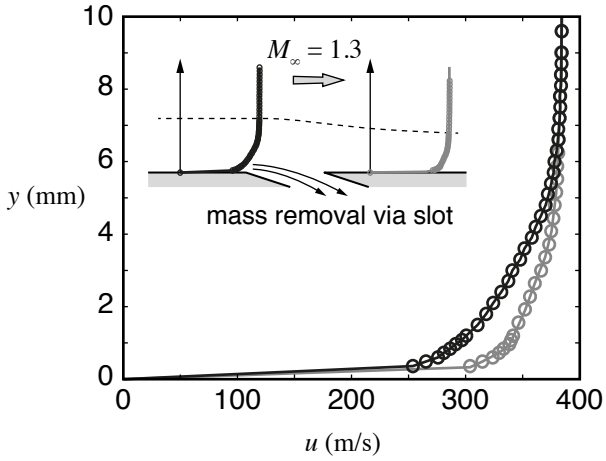

	Pre-slot	Post-slot
$\delta^*_{i,CALC}$	0.727	0.374
$\theta_{i,CALC}$	0.545	0.280
$H_{i,CALC}$	1.34	1.33

Fig. 3 Experimental measurements of boundary layer either side of a suction slot, and the resulting computed integral parameters.

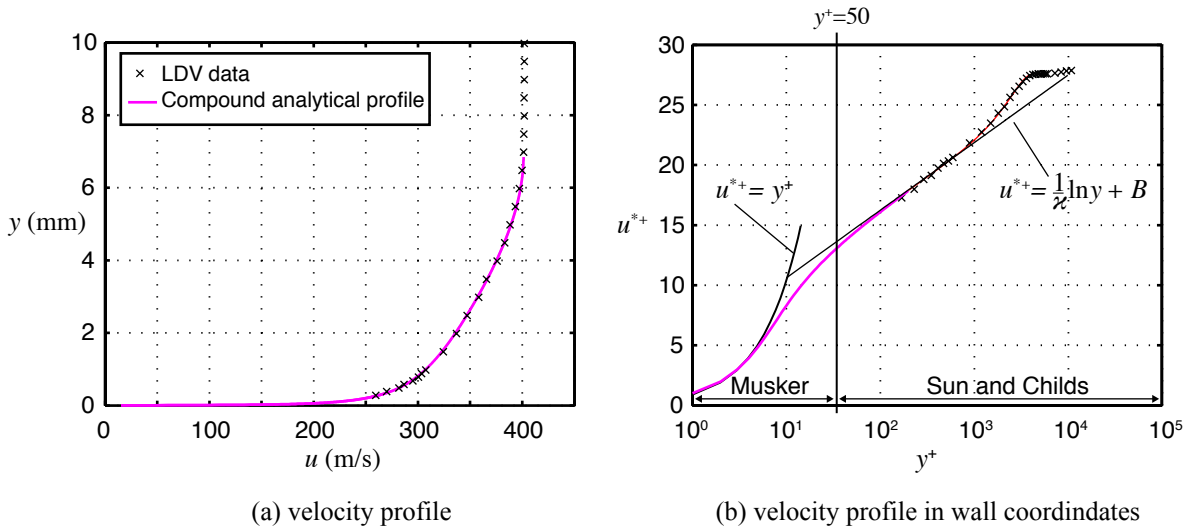

(a) velocity profile (b) velocity profile in wall coordindates

Fig. 4 Experimental data used to generate a relevant analytical equilibrium turbulent boundary layer model: (a) velocity profile; (b) profile in wall coordinates (* indicates van Driest [1951] transformation)

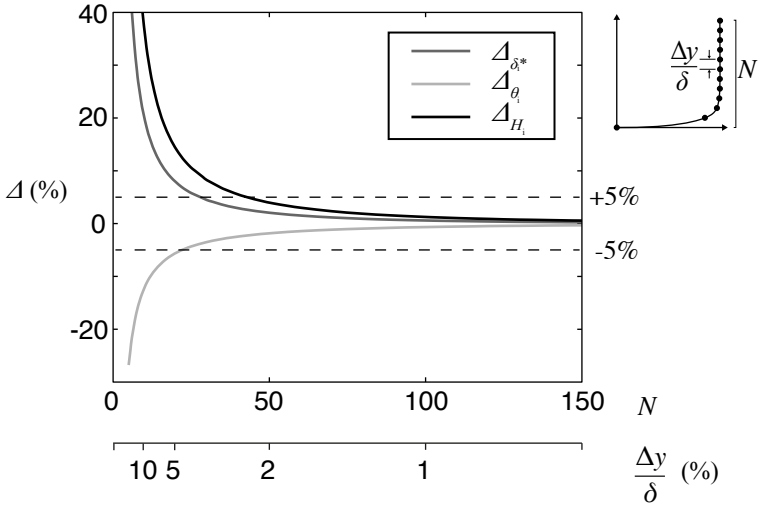

Fig. 5 Error in boundary-layer integral parameters as a function of measurement resolution for H_i = 1.30 boundary layer profile (analytical model)

Table 1 Details of data sets used for error analysis.

Symbol	Type	H_i	Source
○	DNS, M=1.5 shock/boundary layer interaction	1.40–2.80	Pirrozoli et al. 2010
□	DNS, M=2 zero pressure gradient	1.36–1.57	Bernardini et al. 2011, 2011a, 2011b
▽	DNS, M=3 zero pressure gradient	1.40–1.42	Bernardini et al. 2011, 2011a, 2011b
△	DNS, M=4 zero pressure gradient	1.39–1.42	Bernardini et al. 2011, 2011a, 2011b
▼	DNS, zero pressure gradient	1.39–1.53	Schlatter and Orlu 2010
●	DNS, zero pressure gradient	1.52–1.58	Komminaho and Skote 2002
▲	DNS, adverse pressure gradient	1.58–1.99	Komminaho and Skote 2002
■	DNS, zero pressure gradient	1.42–1.67	Spalart 1988
◇	DNS, favourable pressure gradient	1.43–1.54	Spalart 1986
◆	DNS, favourable pressure gradient	1.32–1.38	Marquille et al. 2008
×	Analytical compound model, M = 1.4	1.24–1.36	-

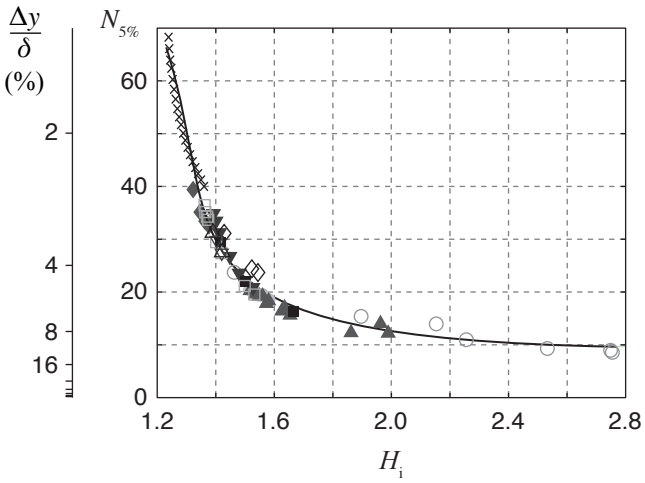

Fig. 6 Critical measurement resolution, $N_{5\%}$, required to give lower than 5% error in all boundary-layer integral parameters (uniform sampling)

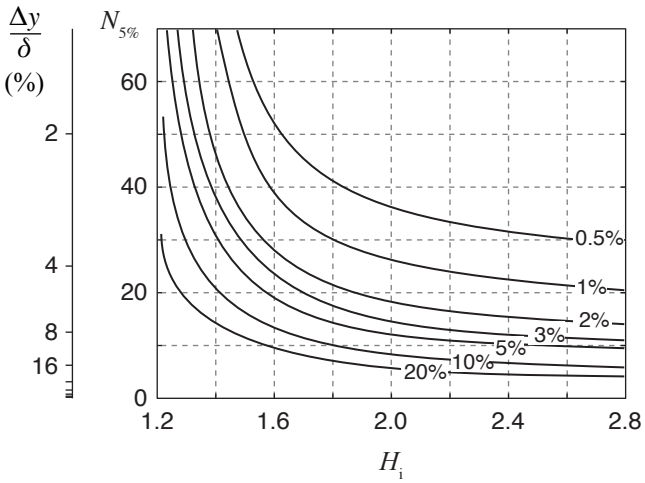

Fig. 7 Curves of critical measurement resolution required to give various error levels in all boundary-layer integral parameters (uniform sampling)

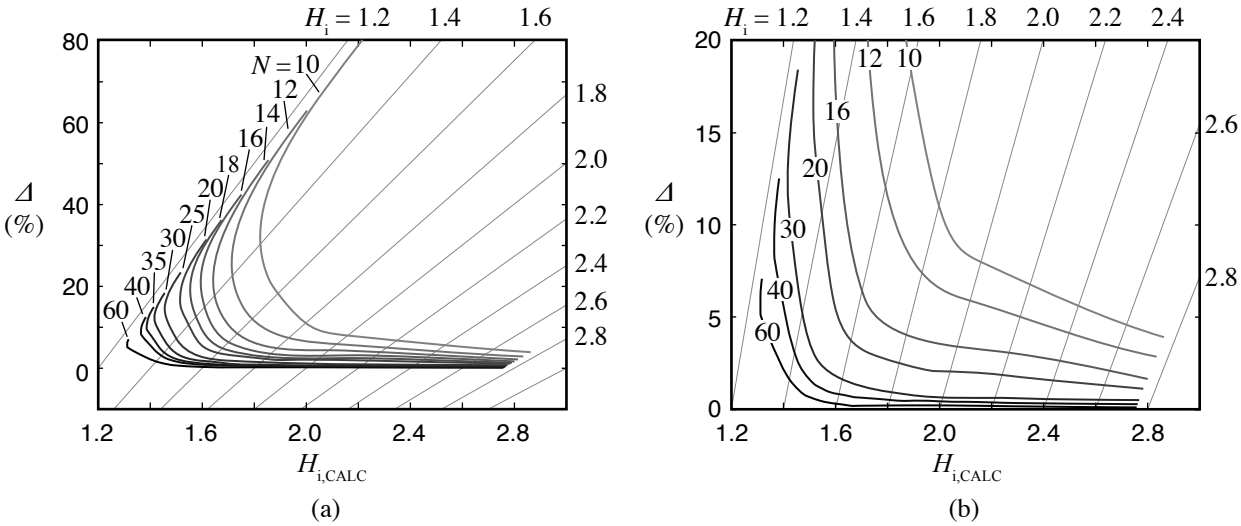

Fig. 8 Errors in boundary-layer integral parameters versus calculated shape factor, H_{iCALC}, for various sample densities: (a) shows the entire range of parameters considered in this paper; (b) shows the same data zoomed in on typical practical values

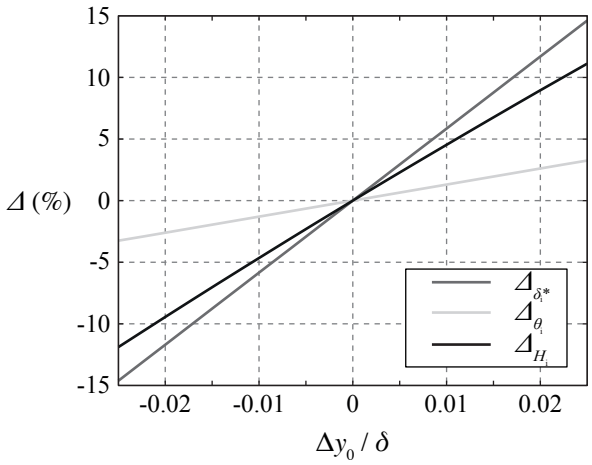

Fig. 9 Error in boundary-layer integral parameters as a function of floor/wall misalignment, $\Delta y_0/\delta$

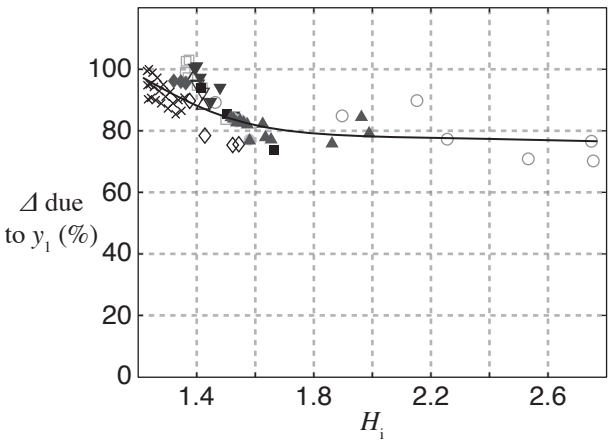

Fig. 10 Percentage of error due to the spacing of the first point from the wall, y_1

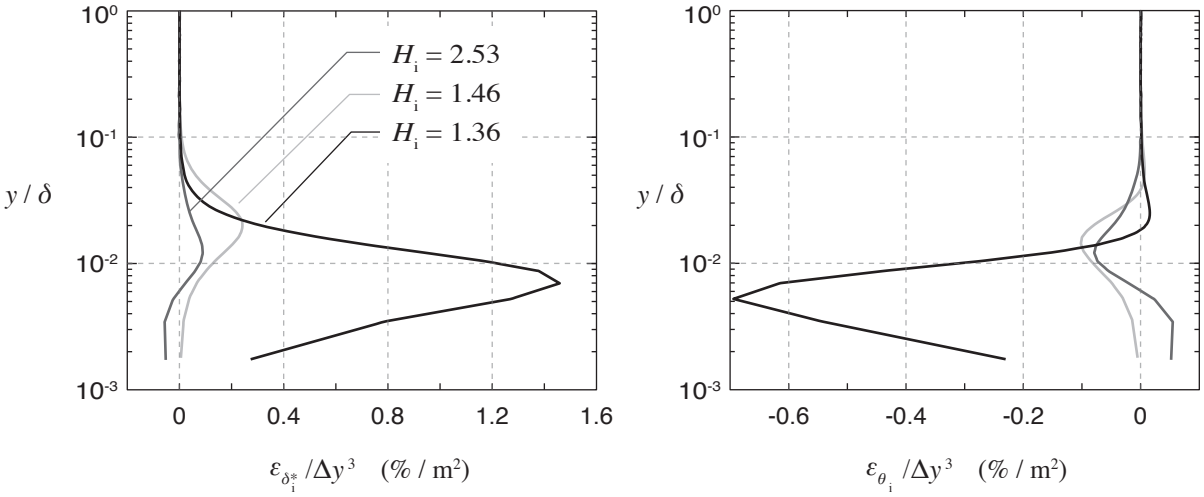

Fig. 11 Wall-normal variation of the error contribution to the displacement thickness, δ_i^*, and momentum thickness, θ_i

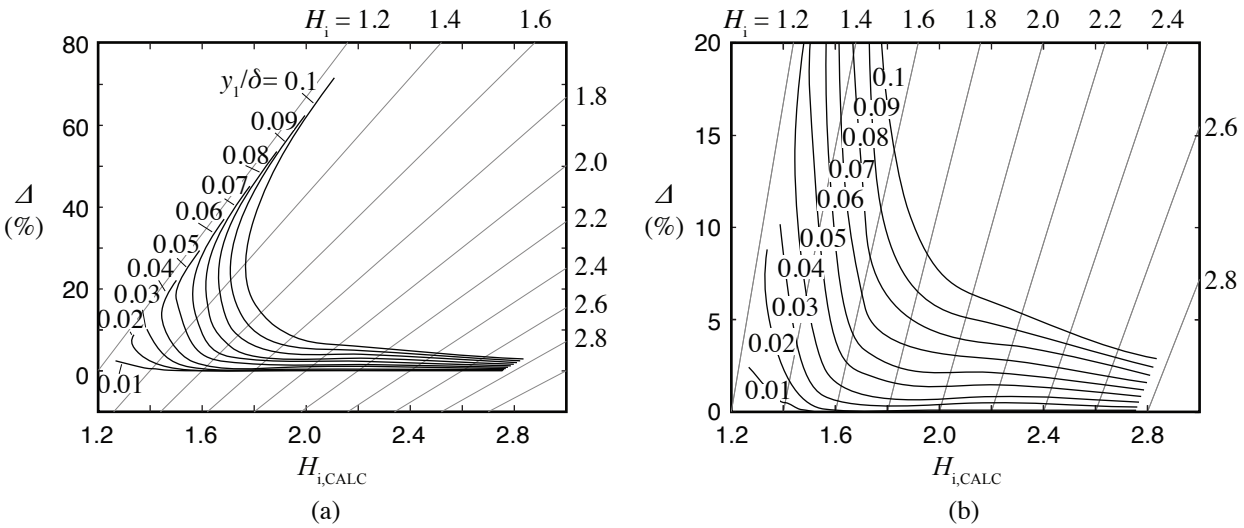

Fig. 12 Errors in integral parameters against calculated value of shape factor H_{iCALC} for various first point spacings y_1. (a) shows the entire range of parameters considered in this paper; (b) shows the same data zoomed in on typical practical values

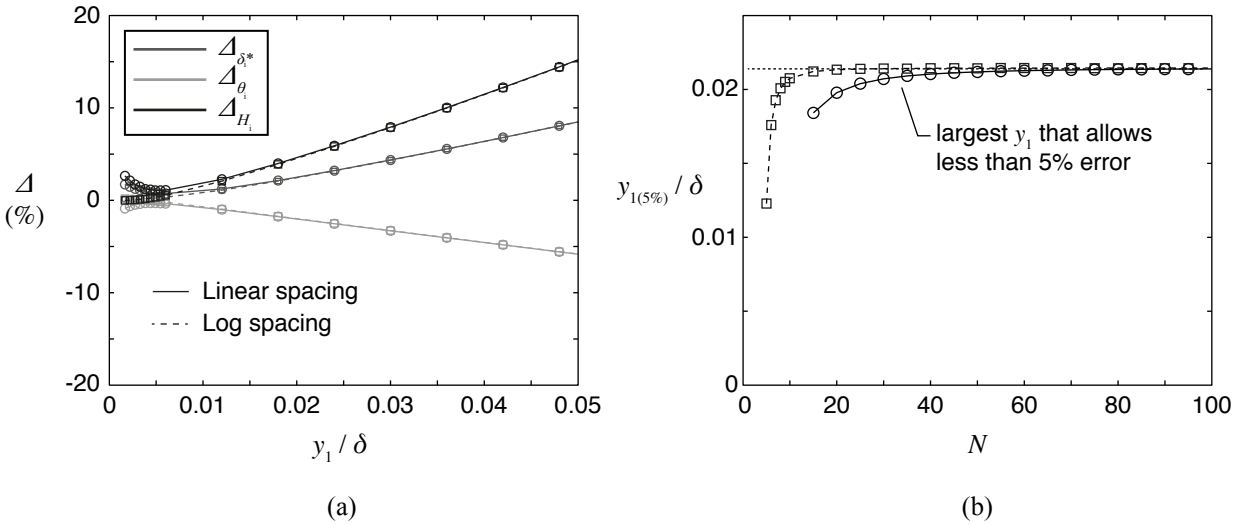

Fig. 13 Comparison of Linear and Logarithmic sampling distributions: solid lines show linearly spaced points; dashed lines show logarithmically spaced points

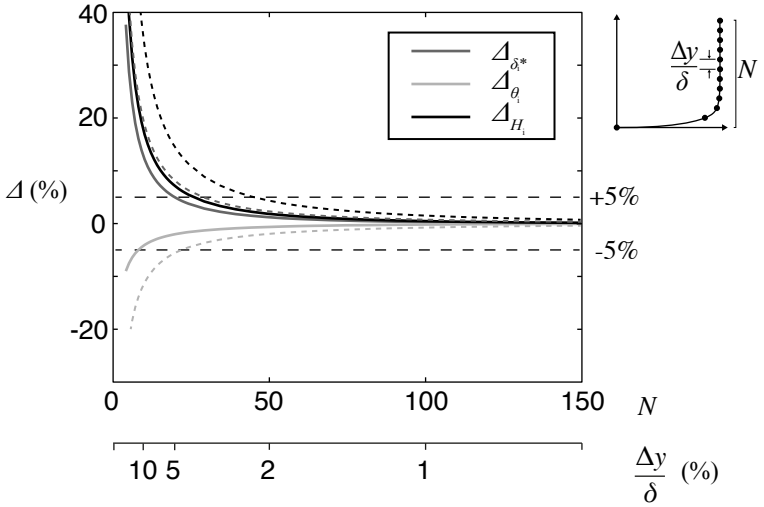

Fig. 14 Variation of error in integral boundary layer parameters with measurement resolution N. Solid lines show the wall modeling method; dashed lines show integration on an unmodified profile, as presented in Figure 5

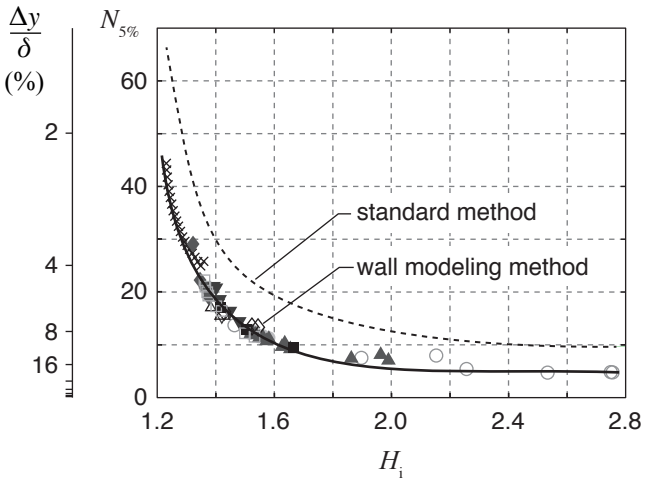

Fig. 15 Measurement resolution required to give better than 5% error in all integral parameters, $N_{5\%}$, versus shape factor H_{i}. Dashed line shows values calculated from unmodified profiles (originally in Figure 6)

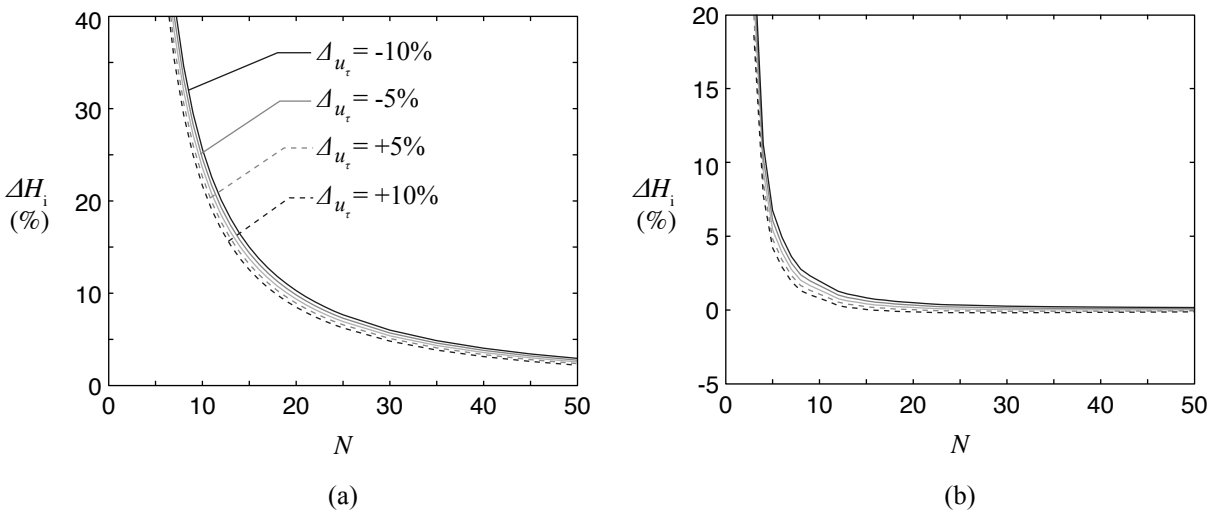

Fig. 16 Error in H_{i} against measurement resolution N for different errors in u_τ used to implement the wall modeling method: (a) profile with H_{i} = 1.30 (analytical); (b) profile with H_{i} = 2.52 (from Pirozzoli et al. [2010])

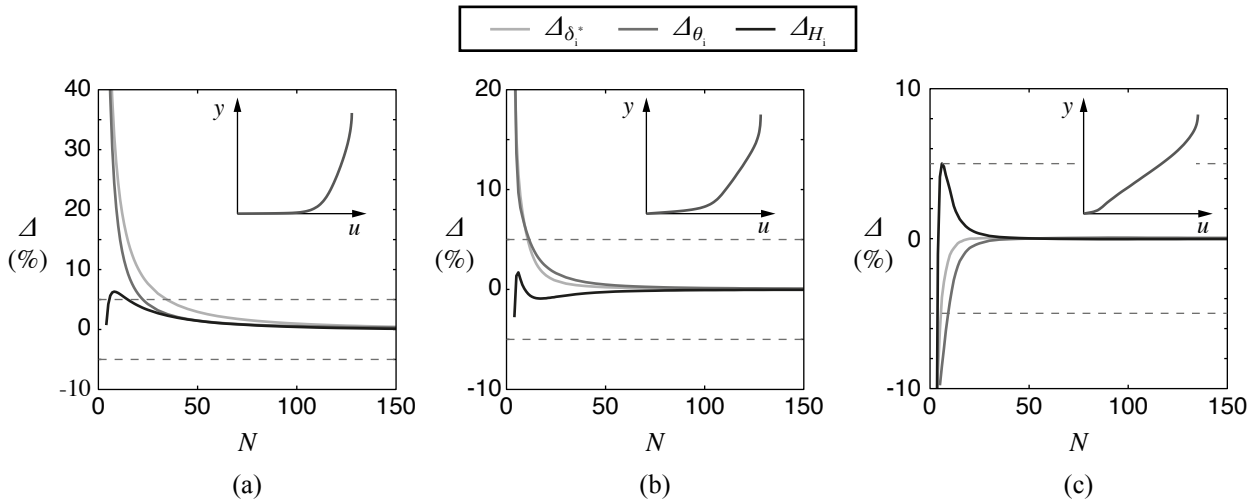

Fig. 17 Variation of error in integral parameters with measurement resolution N using the gradient method for three profiles: (a) $H_i = 1.30$; (b) $H_i = 1.62$ (Komminaho and Skote [2002]); (c) $H_i = 2.52$ (Pirozzoli et al. [2010]). The ±5% error level is indicated by a pair of dashed lines

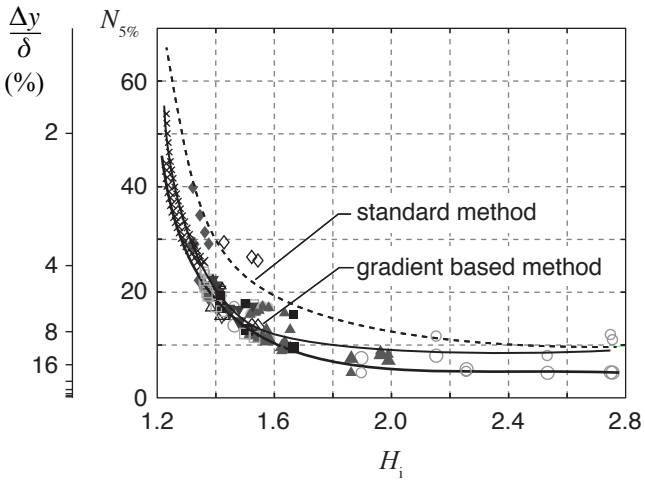

Fig. 18 Measurement resolution required to give better than 5% error in all integral parameters, $N_{5\%}$, versus shape factor, H_i

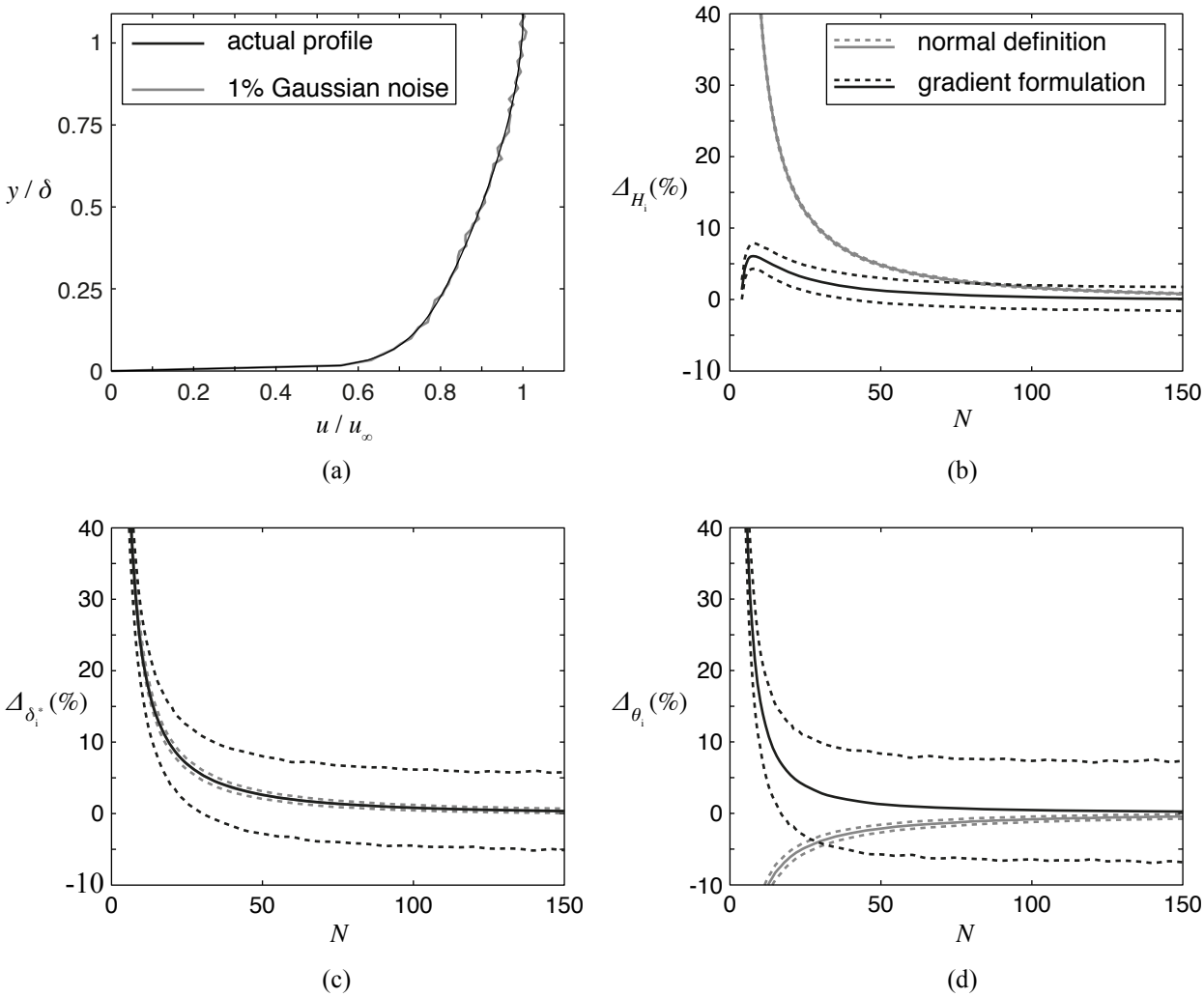

Fig. 19 Effect of noise on the computed integral parameters: (a) test profile, $H_{\mathrm{i}} = 1.30$; (b) error in shape factor, $\Delta_{H_{\mathrm{i}}}$, versus measurement resolution, N; (c) error in displacement thickness, $\Delta_{\delta_{\mathrm{i}}^*}$; (d) error in momentum thickness, $\Delta_{\theta_{\mathrm{i}}}$. Solid lines show the mean error; dashed lines show the standard deviation.

Appendices

A. Numerical integration errors

In Section 2.2 the variation in error incurred due to numerical integration is shown as a function of wall-normal height. For each y this has been estimated by considering the error in the integral between two points around y, $y_1 = y - \Delta y/2$ and $y_2 = y + \Delta y/2$. Let f be a smooth function between the two points y_1 and y_2. The value of the integral $I = \int_{y_1}^{y_2} f \, \mathrm{d}y$ is estimated by numerical integration which involves interpolating between the end points using a curve of order n. The general formula for the error in the resulting value of the integral is given by:

$$\begin{aligned} \varepsilon_I &= \frac{1}{(n+1)!} \frac{\partial^{(n+1)} f}{\partial y^{(n+1)}} \int_{y_1}^{y_2} (\tilde{y} - y_1)(\tilde{y} - y_2) \, \mathrm{d}\tilde{y} \\ &= \frac{1}{(n+1)!} \frac{\partial^{(n+1)} f}{\partial y^{(n+1)}} \left\{ -\frac{1}{6} (y_2 - y_1)^3 \right\} \\ &= -\frac{\Delta y^3}{6(n+1)!} \frac{\partial^{(n+1)} f}{\partial y^{(n+1)}} \end{aligned} \tag{16}$$

For details the reader should refer to Milne-Thomson [1933 reprinted 1951], Delves and Walsh [1974], Nonweiler [1984]. In the present paper, the trapezium rule has been used, which interpolates with straight lines, i.e. $n = 1$. Equation 16 therefore shows that the error will be proportional to the second derivative of f. For the boundary layer integral parameters:

$$\frac{\partial^2 f_{\delta_i^*}}{\partial y^2} = \frac{\partial^2}{\partial y^2} \left(1 - \frac{u}{u_\infty} \right) = -\frac{1}{u_\infty} \frac{\partial^2 u}{\partial y^2} \tag{17}$$

$$\begin{aligned}\frac{\partial^2 f_{\theta_i}}{\partial y^2} &= \frac{\partial^2}{\partial y^2}\left\{\frac{u}{u_\infty}\left(1-\frac{u}{u_\infty}\right)\right\}\\ &= \frac{1}{u_\infty^2}\frac{\partial^2}{\partial y^2}(uu_\infty - u^2)\\ &= \frac{1}{u_\infty^2}\frac{\partial}{\partial y}\left(u_\infty\frac{\partial u}{\partial y} - 2u\frac{\partial u}{\partial y}\right)\\ &= \frac{1}{u_\infty^2}\left((u_\infty - 2u)\frac{\partial^2 u}{\partial y^2} - 2\left(\frac{\partial u}{\partial y}\right)^2\right) .\end{aligned} \tag{18}$$

Inserting Equations 17 and 18 into Equation 16 recovers the quoted formulae, Equations 7 and 8.

B. Gradient-based integral parameters

The integral boundary layer parameters may be redefined in terms of velocity gradients using integration by parts. Starting with the kinematic displacement thickness, δ_i^*, Equation 4: integrating the first term directly and the second term by parts gives:

$$\delta_i^* = \frac{1}{u_\infty}\left([u_\infty y]_0^\infty - \left\{[uy]_0^\infty - \int_0^\infty y\frac{\partial u}{\partial y}\,\mathrm{d}y\right\}\right) .$$

Inserting the boundary conditions, $u(y \to \infty) = u_\infty$ and $u(y = 0) = 0$, enables the first two terms to cancel, leaving the result quoted in equation 14 (section 4.2). Similarly for the kinematic momentum thickness, θ_i, integrating both terms in the integrand of Equation 5 by parts yields

$$\begin{aligned}\theta_i &= \frac{1}{u_\infty^2}\int_0^\infty \left(uu_\infty - u^2\right)\,\mathrm{d}y\\ &= \frac{1}{u_\infty^2}\left\{[u_\infty uy]_0^\infty - \int_0^\infty u_\infty y\frac{\partial u}{\partial y}\,\mathrm{d}y - \left([u^2 y]_0^\infty - 2\int_0^\infty yu\frac{\partial u}{\partial y}\,\mathrm{d}y\right)\right\} .\end{aligned}$$

Again using the boundary conditions, the terms $[u_\infty uy]_0^\infty$ and $[u^2y]_0^\infty$ cancel. Some minor rearrangement leads directly to Equation 15 in section 4.2.

References

P. R Ashill, J. L. Fulker, and K. C. Hackett. A review of recent delevopments in flow control. *Aeronautical Journal*, 109(1095):205–232, 2005.

H. Babinsky, Y. Li, and C. W Pitt-Ford. Microramp control of supersonic oblique shock-wave/boundary-layer interactions. *AIAA Journal*, 47(3):668–675, March 2009.

S. C. C. Bailey, M. Hultmark, J. P. Monty, P. H. Alfredsson, M. S. Chong, R. D. Duncan, J. H. M. Fransson, N. Hutchins, I. Marusic, B. J. McKeon, H. M. Nagib, R. Orlu, A. Segalini, A. J. Smits, and R. Vinuesa. Obtaining accurate mean velocity measurements in high reynolds number turbulent boundary layers using pitot tubes. *Journal of Fluid Mechanics*, 715:642–670, 2013.

M. Bernardini and S. Pirozzoli. Wall pressure fluctuations beneath supersonic turbulent boundary layers. *Physics of Fluids*, 23, 2011a.

M. Bernardini and S. Pirozzoli. Inner/outer layer interactions in turbulent boundary layers: A refined measure for the large-scale amplitude modulation mechanism. *Physics of Fluids*, 23, 2011b.

S. P. Colliss, H. Babinsky, K. Nübler, and T. Lutz. Joint experimental and numerical approach to three-dimensional shock control bump research. *AIAA Journal*, 52(2):432–442, 2014.

D. B. De Graaff and J. K. Eaton. Reynolds-number scaling of the flat-plate turbulent boundary layer. *Journal of Fluid Mechanics*, 422:319–346, 2000.

J.M. Delery. Shock wave/turbulent boundary layer interaction and its control. *Progress in Aerospace Sciences*, 22:209–280, 1985.

L.M. Delves and J. Walsh. *Numerical solutions of integral equations*. Number pg. 13. Clarendon Press, Oxford, 1974.

M. Goodhand and R. Miller. Compressor leading edge spikes: A new performance criterion. *Journal of Turbomachinery*, 133(2), 2010.

E. R. Keener. Boundary-layer measurements on a transonic low-aspect ratio wing. TM 88214, NASA, 1986.

A. Kendall and M. Koochesfahani. A method for estimating wall friction in turbulent wall-bounded flows. *Experiments in Fluids*, 44:773–780, 2008.

J. Komminaho and M. Skote. Reynolds stress budgets in couette and boundary layer flows. *Flow, Turbulence and Combustion*, 68:167–192, 2002.

E. R. Lindgren. Experimental study on turbulent pipe flows of distilled water. Civil Engineering Dept. Report 1AD621071, Oklahoma State University, 1965.

M. Marquillie, J.-P. Laval, and R. Dolganov. Direct numerical simulation of a separated channel flow with a smooth profile. *Journal of Turbulence*, 9(1): 1–23, 2008.

L.M. Milne-Thomson. *The calculus of finite differences*. Number pg. 168. The Macmillan Company, New York and London, 1933 reprinted 1951.

M. V. Morkovin. *Effects of Compressibility on Turbulent Flows*, pages 367–380. M'ecanique de la turbulence. CNRS, 1962.

M. J. Morris, M. Sajben, and J. C. Kroutil. Experimental investigation of normal-shock/turbulent-boundary-layer interactions with and without mass removal. *AIAA Journal*, 30(2):359–366, February 1992.

A. J. Musker. Explicit expression for the smooth wall velocity distribution in a turbulent boundary layer. *AIAA Journal*, 17:655–657, 1979.

T.R.F. Nonweiler. *Computational mathematics: an introduction to numerical approximation*. Number pg. 197. Ellis Horwood, 1984.

R. Örlü, P. Fransson, and P. H. Alfredsson. On near wall measurements of wall bounded flows—the necessity of an accurate determination of the wall position. *Progress in Aerospace Sciences*, 46:353–387, 2010.

S. Pirozzoli and M. Bernardini. Turbulence in supersonic boundary layers at moderate reynolds number. *Journal of Fluid Mechanics*, 688:120–168, 2011.

S. Pirozzoli, M. Bernardini, and F. Grasso. Direct numerical simulation of transonic shock/boundary layer interaction under conditions of incipient separation. *Journal of Fluid Mechanics*, 657:361–393, 2010.

Eduardo Rodriguez-López, Paul J. K. Bruce, and Oliver. R. H. Buxton. A robust post-processing method to determine skin friction in turbulent boundary layers from the velocity profile. *Experiments in Fluids*, 56(68), 2015.

W. G. Sawyer and C. J. Long. A study of normal shock-wave turbulent boundary-layer interactions at mach numbers of 1.3, 1.4, and 1.5. TR 82099, RAE, 1982.

P. Schlatter and R. Örlü. Assessment of direct numerical simulation data of turbulent boundary layers. *Journal of Fluid Mechanics*, 659:116–126, 2010.

P. Spalart. Numerical study of sink flow boundary layers. *Journal of Fluid Mechanics*, 172:307–328, 1986.

P. Spalart. Direct simulation of a turbulent boundary layer up to r_θ = 1410. *Journal of Fluid Mechanics*, 187:61–98, 1988.

P. Spalart and J. H. Watmuff. Experimental and numerical study of a turbulent boundary layer with pressure gradients. *Journal of Fluid Mechanics*, 249: 337–371, 1993.

C. Sun and M. Childs. A modified wall wake velocity profile for turbulent compressible boundary layers. *Journal of Aircraft*, 10(6):381–383, 1973.

N. A. Titchener. *An Experimental Investigation of Flow Control for Supersonic Inlets*. PhD thesis, University of Cambridge, 2013.

E. R. van Driest. Turbulent boundary layer in compressible fluids. *Journal of the Aeronautical Sciences*, 18(3):145–160, 1951.

J.F. Wasserbauer, E. T. Meleason, and P. L. Burstadt. Experimental investigation of the performance of a mach-2.7 two-dimensional bifurcated duct inlet with 30 percent internal contraction. TM 106728, NASA, May 1996.

A. Wheeler, R. Miller, and H. Hodson. The effect of wake induced structures on compressor boundary-layers. *Journal of Turbomachinery*, 129(4):705–712, 2006.

F. M White. *Viscous Fluid Flow*. McGraw-Hill Science, 3 edition, 2006.

K. G. Winter and L. Gaudet. Turbulent boundary-layer studies at high reynolds numbers at mach numbers between 0.2 and 2.8. R&M 3712, Aeronautical Research Council, 1970.

W. F. Wong. The application of boundary layer suction to suppress strong shock-induced separation in supersonic inlets. AIAA-74-1063, October 1974.